9-6-2018

Impaired monocyte cholesterol clearance initiates age-related retinal degeneration and vision loss

Norimitsu Ban

Tae Jun Lee

Abdoulaye Sene

Mayur Choudhary

Michael Lekwuwa

See next page for additional authors

Authors

Norimitsu Ban, Tae Jun Lee, Abdoulaye Sene, Mayur Choudhary, Michael Lekwuwa, Zhenyu Dong, Andrea Santeford, Jonathan B. Lin, Goldis Malek, Daniel S. Ory, and Rajendra S. Apte

JCI insight

Impaired monocyte cholesterol clearance initiates age-related retinal degeneration and vision loss

Norimitsu Ban, … , Daniel S. Ory, Rajendra S. Apte

JCI Insight. 2018;3(17):e120824. https://doi.org/10.1172/jci.insight.120824.

Research Article **Ophthalmology**

Advanced age-related macular degeneration (AMD), the leading cause of blindness among people over 50 years of age, is characterized by atrophic neurodegeneration or pathologic angiogenesis. Early AMD is characterized by extracellular cholesterol-rich deposits underneath the retinal pigment epithelium (RPE) called drusen or in the subretinal space called subretinal drusenoid deposits (SDD) that drive disease progression. However, mechanisms of drusen and SDD biogenesis remain poorly understood. Although human AMD is characterized by abnormalities in cholesterol homeostasis and shares phenotypic features with atherosclerosis, it is unclear whether systemic immunity or local tissue metabolism regulates this homeostasis. Here, we demonstrate that targeted deletion of macrophage cholesterol ABC transporters A1 (ABCA1) and -G1 (ABCG1) leads to age-associated extracellular cholesterol-rich deposits underneath the neurosensory retina similar to SDD seen in early human AMD. These mice also develop impaired dark adaptation, a cardinal feature of RPE cell dysfunction seen in human AMD patients even before central vision is affected. Subretinal deposits in these mice progressively worsen with age, with concomitant accumulation of cholesterol metabolites including several oxysterols and cholesterol esters causing lipotoxicity that manifests as photoreceptor dysfunction and neurodegeneration. These findings suggest that impaired macrophage cholesterol transport initiates several key elements of early human AMD, demonstrating the importance of systemic immunity and aging in promoting disease manifestation. Polymorphisms in genes involved with cholesterol transport and homeostasis […]

JCI insight

RESEARCH ARTICLE

Impaired monocyte cholesterol clearance initiates age-related retinal degeneration and vision loss

Norimitsu Ban,[1] Tae Jun Lee,[1] Abdoulaye Sene,[1] Mayur Choudhary,[2] Michael Lekwuwa,[2] Zhenyu Dong,[1] Andrea Santeford,[1] Jonathan B. Lin,[1,3] Goldis Malek,[2,4] Daniel S. Ory,[5] and Rajendra S. Apte[1,3,6,7]

[1]Department of Ophthalmology and Visual Sciences, Washington University in St. Louis School of Medicine, St. Louis, Missouri, USA. [2]Department of Ophthalmology, Duke University School of Medicine, Durham, North Carolina, USA. [3]Neuroscience Graduate Program, Division of Biology and Biomedical Sciences, Washington University in St. Louis School of Medicine, St. Louis, Missouri, USA. [4]Department of Pathology, Duke University School of Medicine, Durham, North Carolina, USA. [5]Diabetic Cardiovascular Disease Center, [6]Department of Medicine, and [7]Department of Developmental Biology, Washington University in St. Louis School of Medicine, St. Louis, Missouri, USA.

Advanced age-related macular degeneration (AMD), the leading cause of blindness among people over 50 years of age, is characterized by atrophic neurodegeneration or pathologic angiogenesis. Early AMD is characterized by extracellular cholesterol-rich deposits underneath the retinal pigment epithelium (RPE) called drusen or in the subretinal space called subretinal drusenoid deposits (SDD) that drive disease progression. However, mechanisms of drusen and SDD biogenesis remain poorly understood. Although human AMD is characterized by abnormalities in cholesterol homeostasis and shares phenotypic features with atherosclerosis, it is unclear whether systemic immunity or local tissue metabolism regulates this homeostasis. Here, we demonstrate that targeted deletion of macrophage cholesterol ABC transporters A1 (ABCA1) and -G1 (ABCG1) leads to age-associated extracellular cholesterol-rich deposits underneath the neurosensory retina similar to SDD seen in early human AMD. These mice also develop impaired dark adaptation, a cardinal feature of RPE cell dysfunction seen in human AMD patients even before central vision is affected. Subretinal deposits in these mice progressively worsen with age, with concomitant accumulation of cholesterol metabolites including several oxysterols and cholesterol esters causing lipotoxicity that manifests as photoreceptor dysfunction and neurodegeneration. These findings suggest that impaired macrophage cholesterol transport initiates several key elements of early human AMD, demonstrating the importance of systemic immunity and aging in promoting disease manifestation. Polymorphisms in genes involved with cholesterol transport and homeostasis are associated with a significantly higher risk of developing AMD, thus making these studies translationally relevant by identifying potential targets for therapy.

Introduction

Age-related macular degeneration (AMD) is the leading cause of blindness among people over 50 years of age in the industrialized world (1). Early disease is characterized by cholesterol-rich extracellular deposits underneath the retinal pigment epithelium (RPE) called drusen (2–4) or in the subretinal space called subretinal drusenoid deposits (SDD) (5–7). The composition of these deposits is similar to that of atherosclerotic plaques (3). AMD shares several phenotypic characteristics with atherosclerosis, including monocytic inflammation, pathologic angiogenesis, and genetic abnormalities in cholesterol homeostasis (4, 8). Although the molecular mechanisms underlying pathological angiogenesis or RPE atrophy in advanced disease are better understood, there is a paucity of animal models that have been able to recapitulate early human disease — including anatomic features such as thickening of Bruch's membrane (BrM; an acellular lamina underneath the RPE), drusen, or SDD — or functional characteristics such as an association with age, rod photoreceptor dysfunction (9, 10), or impaired dark adaptation (11, 12).

Conflict of interest: The authors have declared that no conflict of interest exists.

Submitted: March 21, 2018
Accepted: July 26, 2018
Published: September 6, 2018

Reference information:
JCI Insight. 2018;3(17):e120824.
https://doi.org/10.1172/jci.insight.120824.

A number of genome-wide association studies (GWAS) have linked AMD to polymorphisms in genes involved in many facets of cholesterol homeostasis such as LIPC, ApoE, ABCA1, and CETP (13, 14). In addition, widespread systemic disturbances in cholesterol metabolism as manifested by altered levels of lipoprotein subtypes have also been associated with AMD (15). Despite reports implicating disruptions in cholesterol homeostasis in mouse models and in human AMD pathogenesis, it has not been established whether it is the systemic immune system or local "eye" cells that regulate cholesterol clearance and the development of the early AMD phenotype. Here, we demonstrate that, in conditional KO mice wherein both *Abca1* and *Abcg1* are deleted in macrophages, there is an age-dependent manifestation of several anatomic and functional AMD disease phenotypes, indicating that cholesterol clearance by macrophages plays a critical role in the early stages of AMD pathogenesis.

Numerous studies have demonstrated that cellular and humoral components of the innate immune system including macrophages, mononuclear phagocytes, and complement proteins contribute to both the development and severity of AMD (16–19). Macrophages not only function as antigen-presenting cells and phagocytic sensors of danger, but they are also important in cholesterol regulation by removing cholesterol from peripheral tissues and transporting it back to the liver through the bloodstream. This process is termed cholesterol efflux or reverse cholesterol transport (RCT) (3), and ABCA1 and ABCG1 play crucial roles in macrophage RCT by effluxing cholesterol from cells to extracellular carriers such as ApoA1 and HDL, respectively (20). In this study, we generated conditional KO mice wherein both *Abca1* and *Abcg1* are deleted in macrophages. We evaluated the retinas structurally by biomicroscopy, histology, and electron microscopy (EM) at 3–12 months of age. In addition, we evaluated retinal function by electrophysiology.

Results

Deletion of Abca1 and Abcg1 in macrophages does not affect the retina at 3 months of age. We have previously reported that mice selectively deficient in *Abca1* in macrophages (*Abca1*$^{fl/fl}$ LysM-Cre–positive [*Abca1*$^{-m/-m}$]) demonstrated increased laser-injury induced choroidal neovascularization (CNV), one of the characteristics of advanced AMD (17). However, when we analyzed treatment-naive *Abca1*$^{-m/-m}$ mice retinas up to 24 months of age, we did not detect any functional abnormalities (Supplemental Figure 1, A–F; supplemental material available online with this article; https://doi.org/10.1172/jci.insight.120824DS1) or biomicroscopic defects (Supplemental Figure 1G) compared with littermate controls (*Abca1*$^{fl/fl}$ Cre–negative; *Abca1*$^{F/F}$) mice. Because *Abca1*$^{-m/-m}$ mice macrophages demonstrated significantly increased *Abcg1* expression (Supplemental Figure 1H), we suspected that ABCG1 might compensate for ABCA1, as both ABCA1 and ABCG1 play crucial roles in macrophage RCT by effluxing cholesterol to extracellular carriers (20). For this reason, and to directly test whether macrophage cholesterol transport regulates the early AMD phenotype, we generated conditional KO mice wherein both *Abca1* and *Abcg1* are deleted in macrophages by crossing *Abca1*$^{fl/fl}$ *and Abcg1*$^{fl/fl}$ mice with LysM-Cre mice (17, 21). The deletion of both genes in macrophages of *Abca1*$^{fl/fl}$ *and Abcg1*$^{fl/fl}$ LysM-Cre positive (*Abca1/g1*$^{-m/-m}$) mice was confirmed by quantitative PCR (qPCR) (Supplemental Figure 2A). We also confirmed that these mice did not carry the *Crb1* gene *rd8* mutation (22) (data not shown). EM at 3 months of age demonstrated large lipid droplets in *Abca1/g1*$^{-m/-m}$ macrophages but not in macrophages of littermate control (*Abca1*$^{fl/fl}$ *and Abcg1*$^{fl/fl}$ Cre negative; *Abca1/g1*$^{F/F}$) mice (Supplemental Figure 2B), consistent with decreased cholesterol efflux in *Abca1/g1*$^{-m/-m}$ macrophages and confirming findings from previous studies (17, 23). However, functional analysis at 3 months of age demonstrated that both scotopic and photopic retinal responses (Figure 1, A–C) and dark adaptation curves recorded from *Abca1/g1*$^{-m/-m}$ mice retinas were normal (Figure 1D). In addition, in vivo imaging and histological examination of retinal sections of *Abca1/g1*$^{-m/-m}$ mice did not show any substantial differences (Figure 1, E and F). These results suggest that deletion of both ABCA1 and ABCG1 in macrophages does not affect retinal function, vision, or morphology acutely or at a young age.

Abca1/g1$^{-m/-m}$ *mice demonstrate RPE abnormalities, BrM thickening, and impaired dark adaptation at 6 months of age*. In order to simulate the human condition, we aged *Abca1/g1*$^{-m/-m}$ mice and their littermate controls. Upon analysis at 6 months age, we found that scotopic a-waveforms were now slightly attenuated in *Abca1/g1*$^{-m/-m}$ retinas compared with littermate controls, confirming scotopic rod photoreceptor dysfunction (Figure 2, A–C). In addition, 6-month-old *Abca1/g1*$^{-m/-m}$ eyes showed impaired dark adaptation (Figure 2D), consistent with the dysfunction of RPE cells. Notably, this combination of rod photoreceptor dysfunction and impaired dark adaptation is a key feature of early and intermediate AMD (9–12). Ultrastructural histology revealed disrupted RPE structure with accumulation of lipid globules in the eyes of *Abca1/g1*$^{-m/-m}$ mice but not in littermate controls (Figure 2E

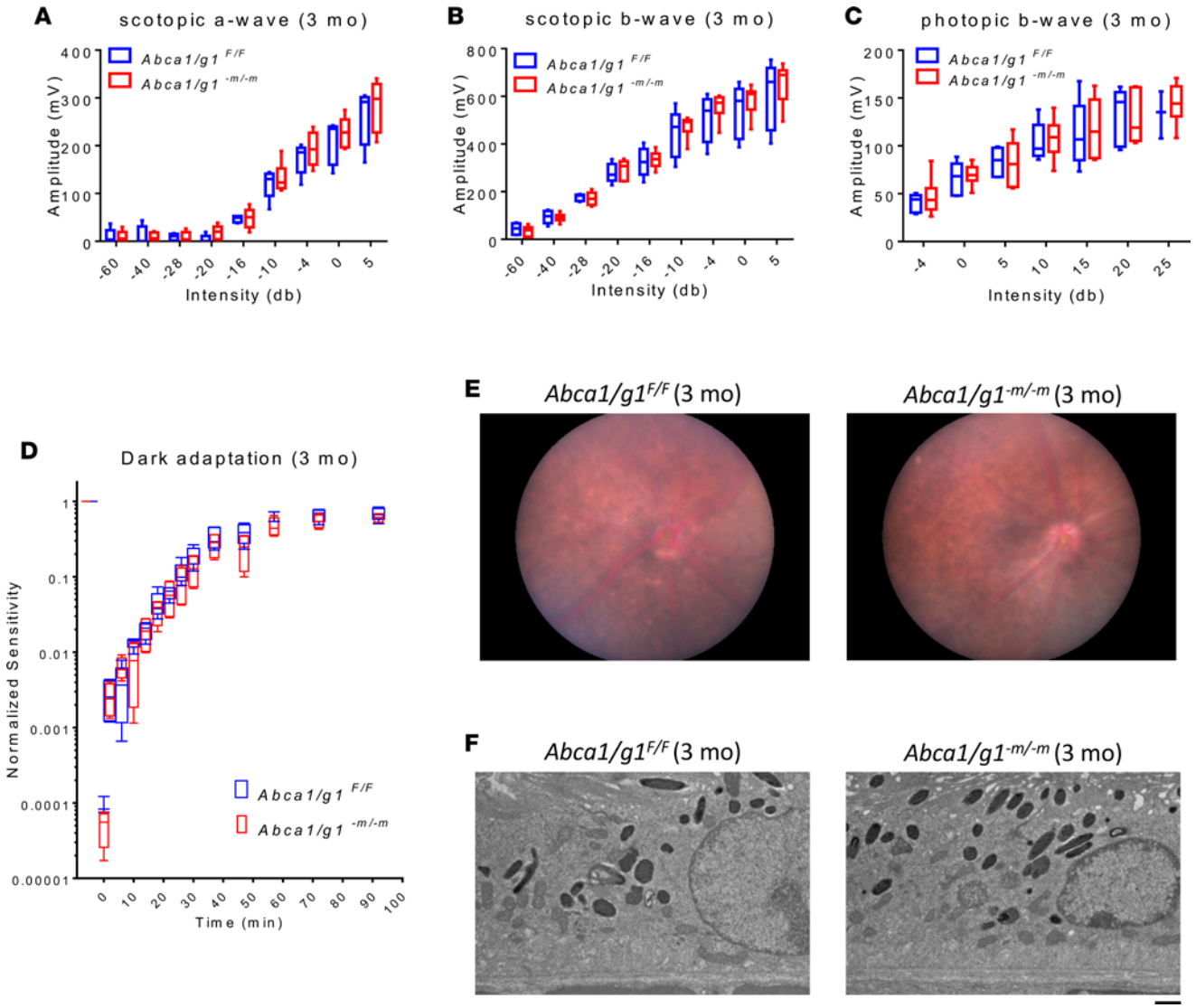

Figure 1. Three-month-old *Abca1/g1*$^{-m/-m}$ retinas do not show functional deficits or morphological abnormalities in the retina and RPE. (**A–C**) Electroretinography (ERG) of 3-month-old *Abca1/g1*$^{F/F}$ (n = 5) and *Abca1/g1*$^{-m/-m}$ mice (n = 6). (**A**) Scotopic a-wave amplitude. (**B**) Scotopic b-wave amplitude. (**C**) Photopic b-wave amplitude. No significant difference was detected by 2-way ANOVA. (**D**) Dark adaptation curves of 3-month-old *Abca1/g1*$^{F/F}$ (n = 5) and *Abca1/g1*$^{-m/-m}$ mice (n = 4). No significant difference was detected by 2-way ANOVA. (**E**) Representative fundus images of 3-month-old *Abca1/g1*$^{F/F}$ and *Abca1/g1*$^{-m/-m}$ mice. (**F**) Representative electron microscopy images of 3-month-old *Abca1/g1*$^{F/F}$ and *Abca1/g1*$^{-m/-m}$ mice retinal pigmented epithelium (RPE). Scale bar: 1 μm. Values are mean ± SEM.

and Supplemental Figure 3). *Abca1/g1*$^{-m/-m}$ mice RPE also showed increased BrM thickening (Figure 2, F and G), which is another morphological characteristic of human eyes with AMD.

Retinal neurodegeneration of Abca1/g1$^{-m/-m}$ *mice increases in severity and affects cone photoreceptors at 12 months of age*. We next examined whether further aging would recapitulate additional features of human AMD in the mouse eye. At 12 months of age, both scotopic a- and b-waveforms were significantly attenuated in *Abca1/g1*$^{-m/-m}$ retinas compared with littermate controls (Figure 3, A and B), confirming additional rod neurodegeneration. In addition, photopic responses were also significantly attenuated (Figure 3C), suggesting cone photoreceptor dysfunction. Dark adaptation was also further impaired (Figure 3D). Biomicroscopic examination of *Abca1/g1*$^{-m-/m}$ eyes now showed yellowish white lesions scattered throughout the retina (Figure 3E).

Subretinal deposits of Abca1/g1$^{-m/-m}$ *mice progressively increase in number with age*. The yellowish white lesions throughout the retina corresponded to hyperreflective outer retinal focal deposits underneath the neurosensory retina on optical coherence tomography (OCT) imaging (Figure 4A). Quantitative analysis of these SD in *Abca1/g1*$^{-m-/m}$ mice showed progressive increase with age, with a significant number of SD

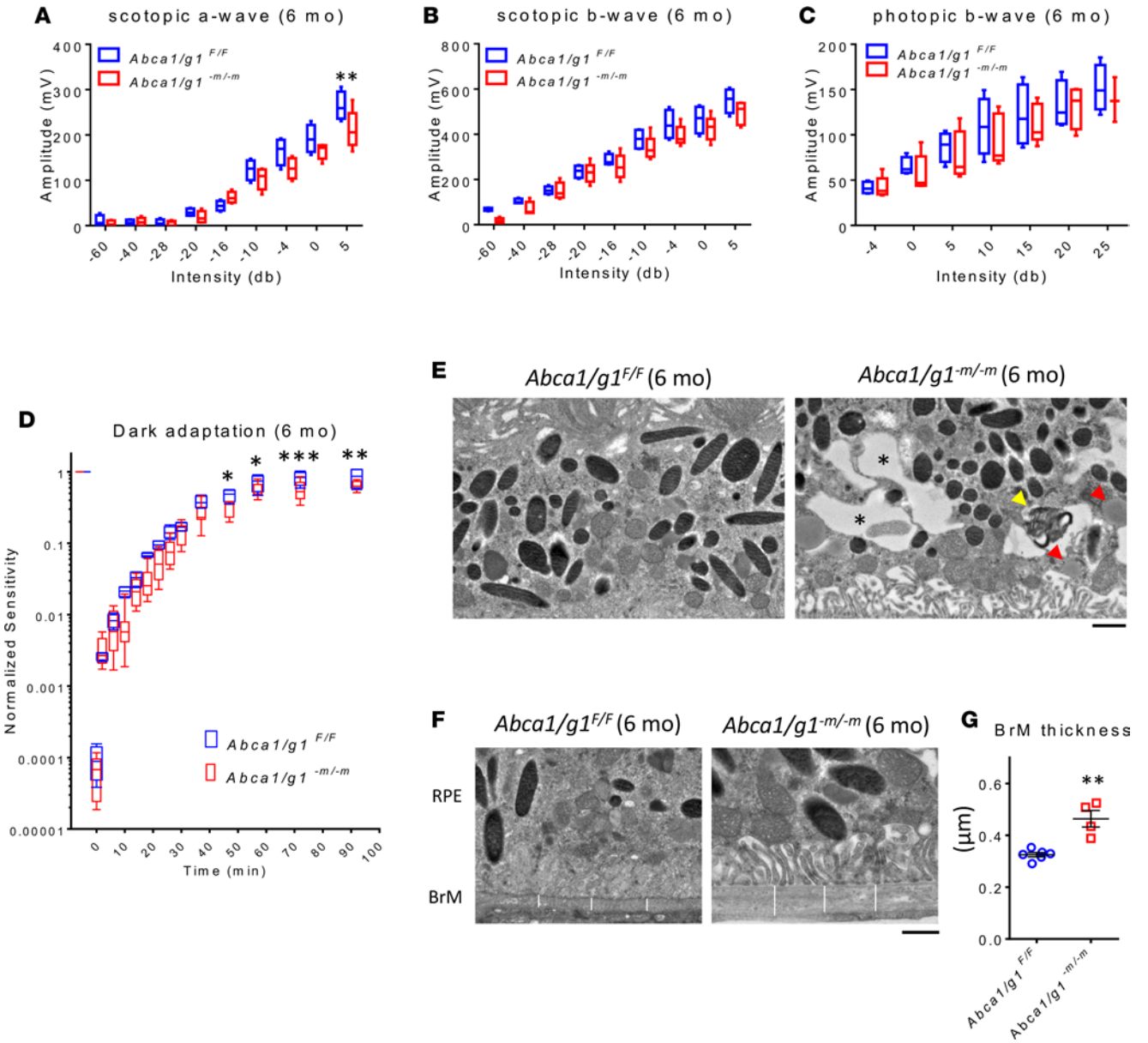

Figure 2. Six-month-old *Abca1/g1*$^{-m/-m}$ retinas demonstrate decreased scotopic responses and impaired dark adaptation associated with disrupted RPE morphology and Bruch's membrane thickening. (**A–C**) ERG of 6-month-old *Abca1/g1*$^{F/F}$ (n = 4) and *Abca1/g1*$^{-m/-m}$ mice (n = 5). (**A**) Scotopic a-wave amplitude. (**B**) Scotopic b-wave amplitude. (**C**) Photopic b-wave amplitude. $^{**}P < 0.01$ by 2-way ANOVA with post hoc Bonferroni's multiple comparison test. (**D**) Dark adaptation curves of 6-month-old *Abca1/g1*$^{F/F}$ (n = 4) and *Abca1/g1*$^{-m/-m}$ mice (n = 8). $^{*}P < 0.05$, $^{**}P < 0.01$, and $^{***}P < 0.001$ by 2-way ANOVA with post hoc Bonferroni's multiple comparison test. (**E** and **F**) Representative electron microscopy images of 6-month-old *Abca1/g1*$^{F/F}$ and *Abca1/g1*$^{-m/-m}$ mice retinal pigmented epithelium (RPE). (**E**) Illustration of dysmorphic changes in 6-month-old *Abca1/g1*$^{F/F}$ and *Abca1/g1*$^{-m/-m}$ mice RPE. Note the vacuoles (asterisks), photoreceptor disk fragments (yellow arrowhead), and lipid droplets (red arrowheads) in *Abca1/g1*$^{-m/-m}$ mice RPE. Scale bar: 1 μm. (**F**) Thickness change of 6-month-old *Abca1/g1*$^{F/F}$ (n = 6) and *Abca1/g1*$^{-m/-m}$ (n = 4) mice Bruch's membrane (BrM). Note the white bars, which represent BrM thickness. Scale bar: 1 μm. (**G**) Quantification of BrM thickness. $^{**}P < 0.01$ by 2-tailed unpaired t test. Values are mean ± SEM.

by 12 months of age compared with littermate controls (Figure 4B). EM confirmed that the deposits were subretinal and contained lipid globules, degenerative vacuoles, and cellular debris (Figure 4C). Some SD were associated with infiltration of mononuclear cells (Figure 4C).

Infiltrating cells in the subretinal space are Iba1- or F4/80-positive monocytic cells. To investigate the identity of the cellular component of SD, we performed IHC with a monocyte/microglial marker (Iba1), as well as qPCR of the retina/RPE/choroid complex. The number of Iba1-positive cells in the subretinal space, visualized by IHC, were significantly increased at 12 months of age in *Abca1/g1*$^{-m/-m}$ mice (Figure 5, A and B). Increased *Iba1* expression was also confirmed in the retina/RPE/choroid complex of

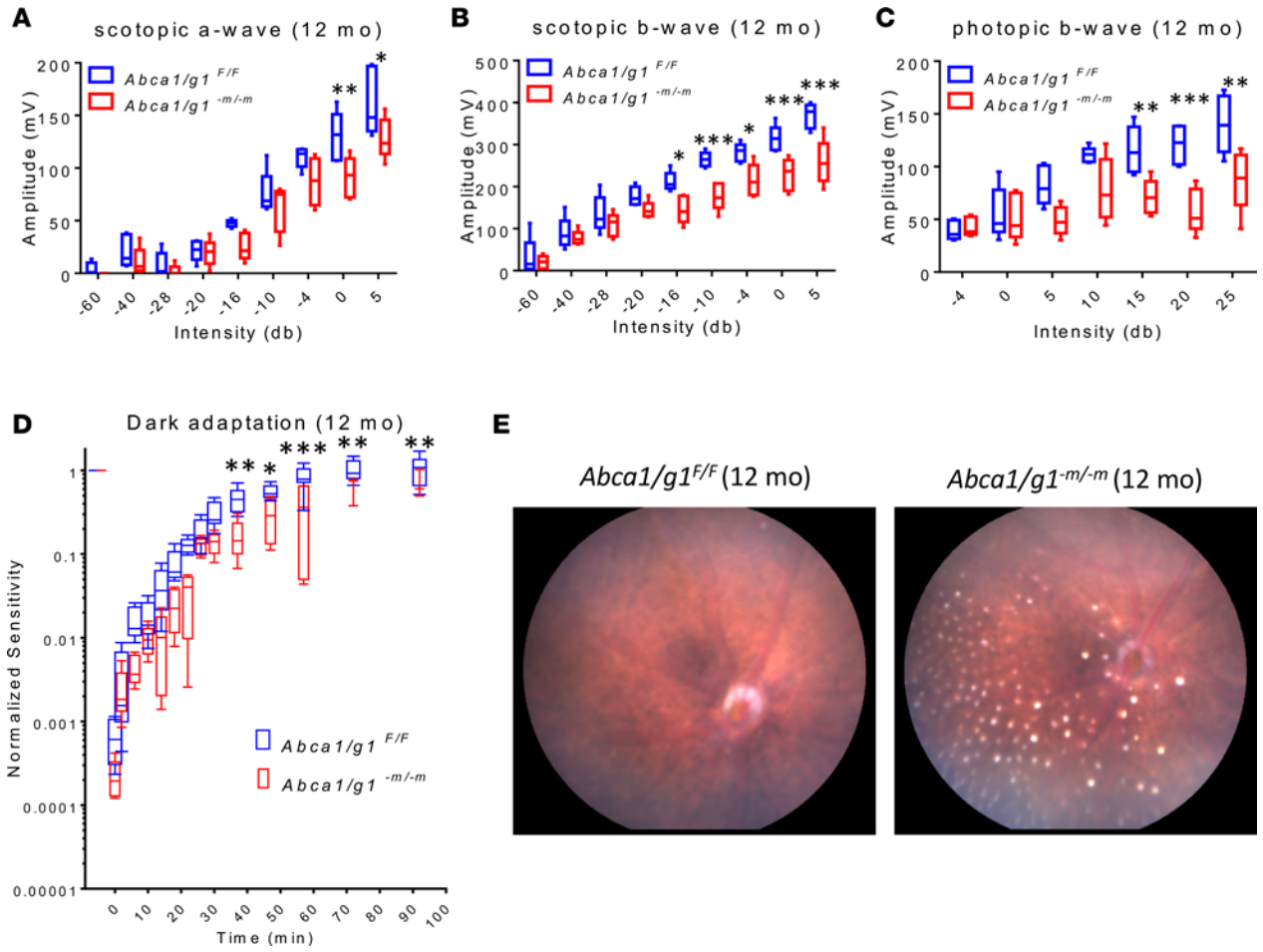

Figure 3. Neurodegeneration of aged *Abca1/g1*$^{-m/-m}$ (12-month-old) retinas increases in severity and extends to photopic dysfunction with significant subretinal deposits. (**A**–**C**) Electroretinography (ERG) of 12-month-old *Abca1/g1*$^{F/F}$ (n = 5) and *Abca1/g1*$^{-m/-m}$ mice (n = 5). (**A**) Scotopic a-wave amplitude. (**B**) Scotopic b-wave amplitude. (**C**) Photopic b-wave amplitude. *P < 0.05, **P < 0.01, and ***P < 0.001 by 2-way ANOVA with post hoc Bonferroni's multiple comparison test. (**D**) Dark adaptation curves of 12-month-old *Abca1/g1*$^{F/F}$ (n = 8) and *Abca1/g1*$^{-m/-m}$ (n = 5). *P < 0.05, **P < 0.01, and ***P < 0.001 by 2-way ANOVA with post hoc Bonferroni's multiple comparison test. (**E**) Representative fundus images of 12-month-old *Abca1/g1*$^{F/F}$ and *Abca1/g1*$^{-m/-m}$ mice retinas. Note the white yellowish dots of *Abca1/g1*$^{-m/-m}$ mice retinas.

Abca1/g1$^{-m/-m}$ mice by qPCR (Figure 5C). IHC with another monocyte/microglial marker (F4/80) also showed increased F4/80-positive cells in the subretinal space (Figure 5, D and E). Increased *F4/80* expression was also confirmed in the retina/RPE/choroid complex of *Abca1/g1*$^{-m/-m}$ mice by qPCR (Figure 5F). These results indicate that infiltrating cells in the subretinal space are likely macrophages/microglia. Recent histological analysis of human SDD describes the presence of bloated macrophage clusters in these lesions (7). As such, SD of old *Abca1/g1*$^{-m/-m}$ mice are phenotypically similar to SDD seen in human AMD.

Aged Abca1/g1$^{-m/-m}$ *mice demonstrate lipid accumulation underneath the retina and within RPE.* We further analyzed 12-month-old *Abca1/g1*$^{-m/-m}$ mice for the precise distribution of lipid deposits and for specific composition. Oil Red O (ORO) staining demonstrated focal lipid accumulations within the RPE, as well as in the subretinal space (Figure 6A), consistent with the findings on EM ultrastructural analysis. Analysis of the retina/RPE/choroid complex by liquid chromatography–tandem mass spectrometry (LC-MS/MS) revealed increased free cholesterol and several cholesterol metabolites (3β,5α,6β-cholestanetriol [C-triol] and 4β-hydroxycholesterol [4β-HC]) (Figure 6B), as well as several cholesterol ester species (Figure 6C). These findings demonstrate that the SD and lipids within RPE are composed of cholesterol and cholesterol esters, as well as cholesterol oxidation products that suggest a highly oxidative environment within the lipid deposits.

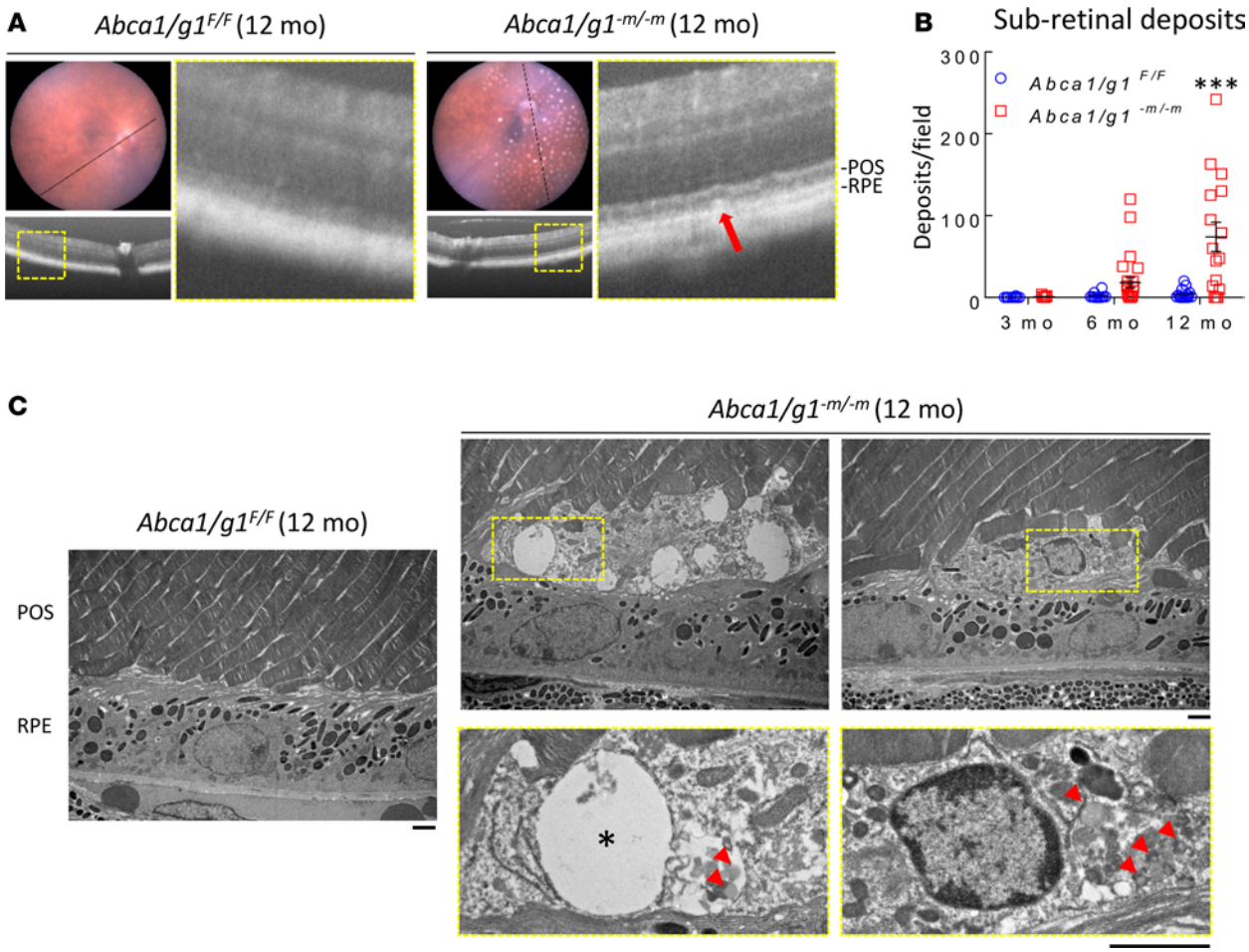

Figure 4. Subretinal deposits contain lipid globules and degenerative vacuoles. (**A**) Representative optical coherence tomography (OCT) images of 12-month-old *Abca1/g1*$^{F/F}$ and *Abca1/g1*$^{-m/-m}$ mice retinas. Note the subretinal hyperreflective deposits in *Abca1/g1*$^{-m/-m}$ mice retinas (red arrow) corresponding to fundus yellowish white dots. POS, photoreceptor outer segment. (**B**) Quantification of subretinal deposits in 3-, 6-, and 12-month-old *Abca1/g1*$^{F/F}$ and *Abca1/g1*$^{-m/-m}$ mice retinas. *Abca1/g1*$^{F/F}$, n = 10, 10, and 15; *Abca1/g1*$^{-m/-m}$, n = 13, 24, and 16, respectively. ***$P < 0.001$ by 2-way ANOVA with post hoc Bonferroni's multiple comparison test. (**C**) Representative electron microscopy images of 12-month-old *Abca1/g1*$^{F/F}$ and *Abca1/g1*$^{-m/-m}$ mice retinas. Note the vacuoles (asterisk) and lipid globules (red arrowheads) within the subretinal deposit in *Abca1/g1*$^{-m/-m}$ mice retinas. Scale bar: 1 μm. Values are mean ± SEM.

Discussion

Here, we have demonstrated that, in conditional KO mice wherein macrophage cholesterol efflux capacities are disabled (*Abca1/g1*$^{-m/-m}$), there is an age-dependent manifestation of several early and intermediate anatomic AMD disease phenotypes, including cellular and noncellular SD similar to SDD, increased BrM thickening, and accumulation of free cholesterol, cholesterol metabolites, and cholesteryl esters. In addition, KO mice demonstrate several key features of early functional degradation seen in human AMD, including impaired dark adaptation and rod photoreceptor dysfunction.

Although we generated macrophage-specific conditional KO mice by crossing *Abca1*$^{fl/fl}$ and *Abcg1*$^{fl/fl}$ mice with LysM-Cre mice, it has been established that LysM-Cre promotes significant deletion not only in macrophages, but also in neutrophils (24). A previous study demonstrated variable deletion of *Abca1* and *Abcg1* in neutrophils (25). Thus, we cannot exclude the possibility that the deletion of *Abca1* and *Abcg1* in neutrophils might also affect the retinal phenotype. However, in addition to the fact that macrophages, but not neutrophils, play crucial roles in RCT from tissues, we demonstrated increased gene expression of macrophage markers *Iba1* and *F4/80*, but not the neutrophil marker *Gr-1*, in the eyes of 12-month-old *Abca1/g1*$^{-m/-m}$ mice (Supplemental Figure 4). For these reasons, we conclude that the retinal phenotypes we observed at 12 months of age are mainly associated with dysfunctional *Abca1*- and *Abcg1*-deficient macrophages, although further study might elucidate this more precisely.

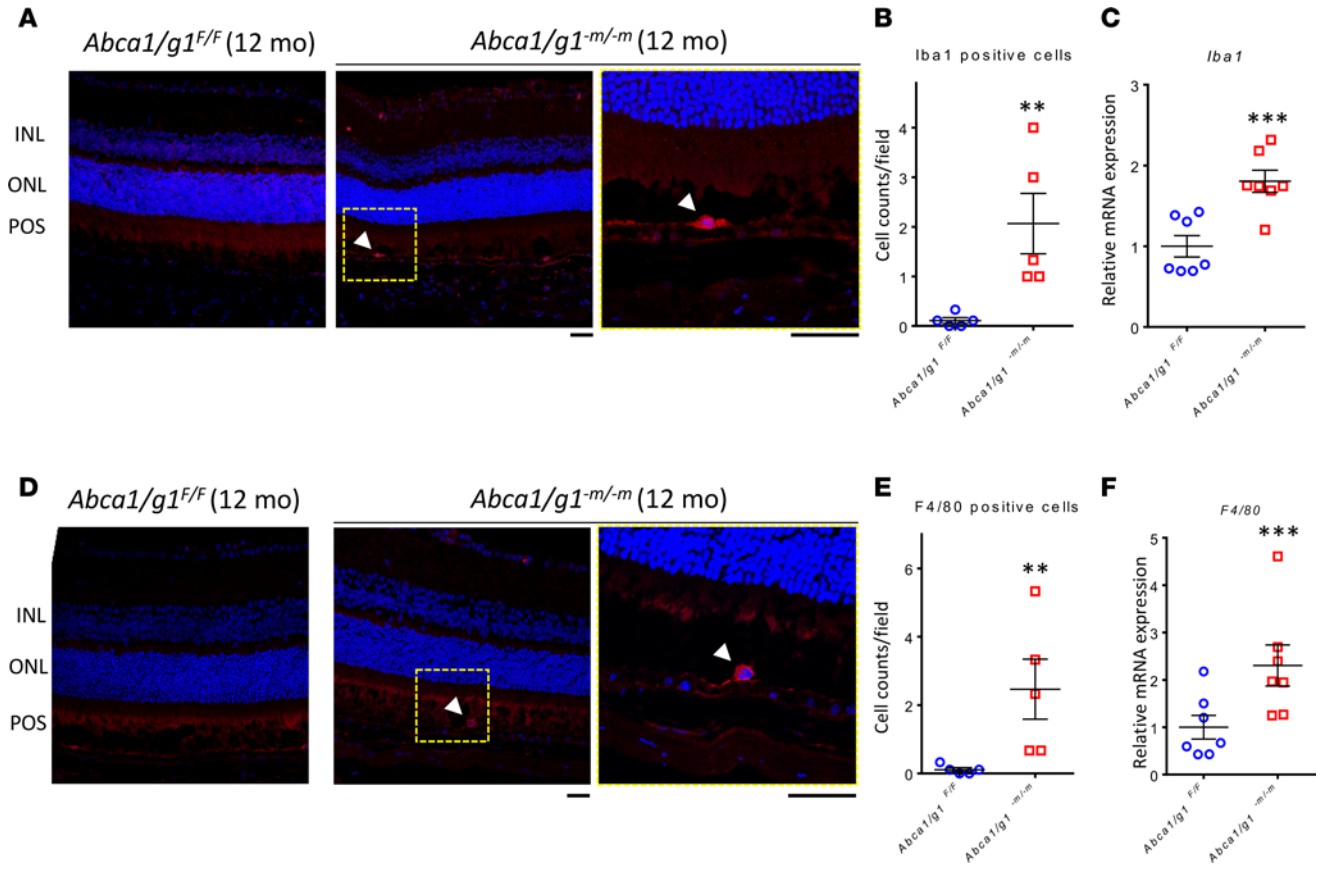

Figure 5. Infiltrated cells in subretinal space are IBA1 and F4/80 positive. (**A**) Representative Iba1 IHC staining of 12-month-old *Abca1/g1*$^{F/F}$ and *Abca1/g1*$^{-m/-m}$ mice retinas. Red, Iba1; blue, DAPI. Scale bar: 50 μm. INL, inner nuclear layer; ONL, outer nuclear layer; POS, photoreceptor outer segment. (**B**) Quantification of Iba1-positive cells in subretinal space. *Abca1/g1*$^{F/F}$, *n* = 5; *Abca1/g1*$^{-m/-m}$, *n* = 5. $^{**}P < 0.01$ by 2-tailed Mann-Whitney *U* test. (**C**) qPCR quantification of *Iba1* expressions in the retina/RPE/choroid complex. *Abca1/g1*$^{F/F}$, *n* = 7; *Abca1/g1*$^{-m/-m}$, *n* = 7. $^{***}P < 0.001$ and by 2-tailed unpaired *t* test. (**D**) Representative IHC staining of 12-month-old *Abca1/g1*$^{F/F}$ and *Abca1/g1*$^{-m/-m}$ mice retinas. Red, F4/80; blue, DAPI. Scale bar: 50 μm. (**E**) Quantification of F4/80-positive cells in the subretinal space. *Abca1/g1*$^{F/F}$, *n* = 5; *Abca1/g1*$^{-m/-m}$, *n* = 5. $^{**}P < 0.01$ and by 2-tailed Mann-Whitney test. (**F**) qPCR quantification of *F4/80* expressions in the retina/RPE/choroid complex. *Abca1/g1*$^{F/F}$, *n* = 7; *Abca1/g1*$^{-m/-m}$, *n* = 7. $^{***}P < 0.001$ and by 2-tailed unpaired *t* test. Values are mean ± SEM.

Polymorphisms in genes involved with cholesterol transport and homeostasis are associated with a significantly higher risk of developing AMD (13, 14), thus making these studies translationally relevant by identifying potential targets for therapy. Although there are no previous reports of ABCG1 polymorphisms associated with increased AMD risk, we found that, in *Abca1*$^{-m/-m}$ mice, ABCG1 might compensate for the lack of ABCA1. As such, we wanted to effectively neutralize the efflux pathway by the deletion of both *Abca1* and *Abcg1* in order to examine its effect on the retinal phenotype with aging.

We are also aware that ABCA1 polymorphisms associated with AMD risk are HDL elevating (26–30). HDL carrier capacity is not just limited by level but by the size and quality of the particles available at the retinal choroidal interphase. In addition, these findings also suggest that there is a complex interplay between systemic lipid profiles and local lipid profiles in AMD.

Although we are proposing our mouse model as an early-stage AMD model, an important feature of AMD that is lacking in this model is the development of sub-RPE drusen and may represent metabolic differences between the mouse and human retina and RPE. However, although our mouse model (*Abca1/g1*$^{-m/-m}$ mice) does not demonstrate all the features of human disease, age is a key variable here, just as in human AMD that only affects people over the age of 50 years. Thus, these findings suggest that maintenance of cholesterol homeostasis and macrophage-mediated cholesterol efflux may be critical pathways that initiate the development of AMD. These pathways deserve further investigation in order to determine whether pharmacotherapeutic interventions targeting these pathways, either locally or systemically, might prove efficacious in either preventing the development of early AMD or the progression to advanced stages of disease where vision loss is imminent.

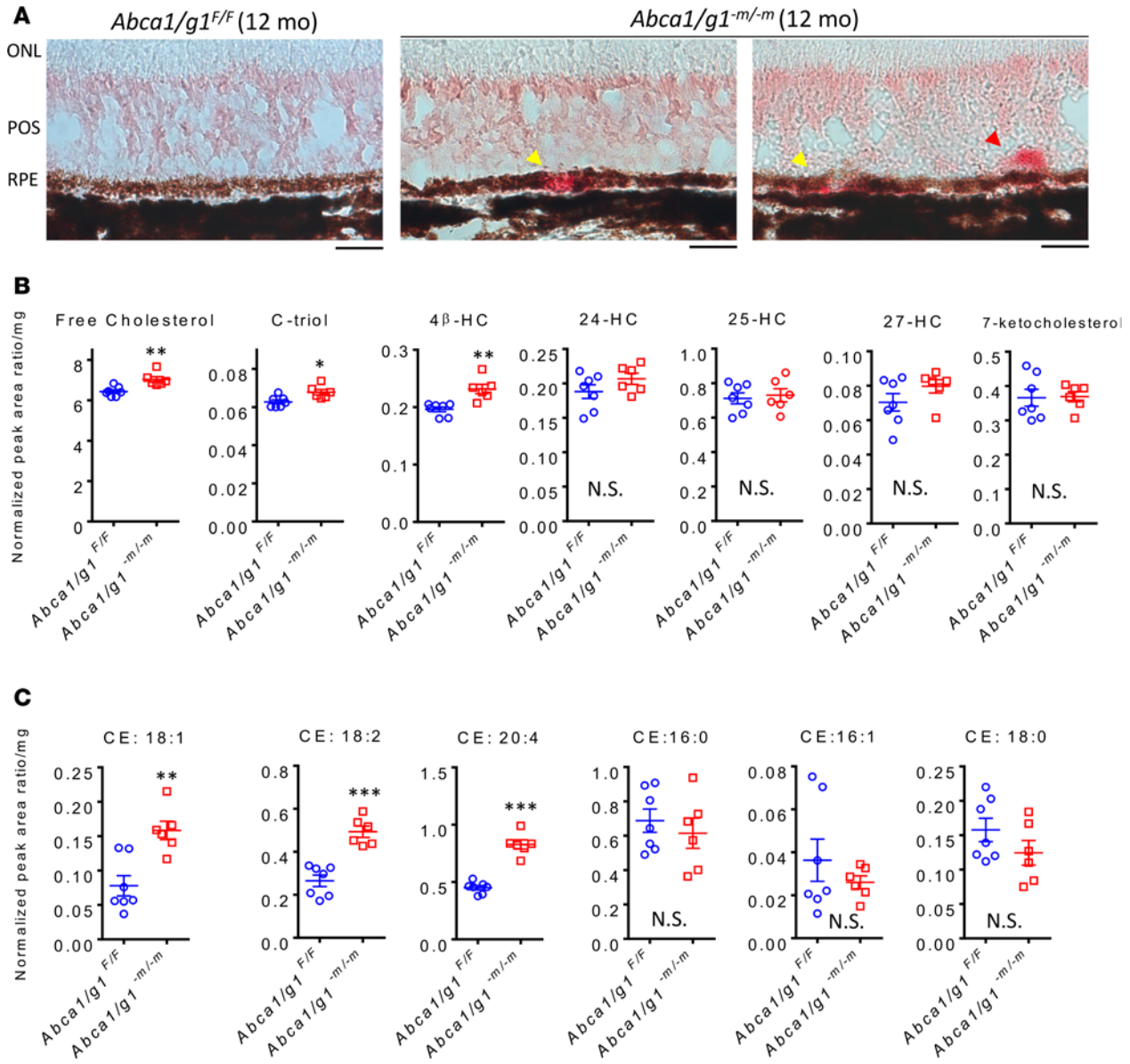

Figure 6. Lipid analysis of *Abca1/g1*$^{-m/-m}$ mice eyes at 12 months of age demonstrates focal subretinal and RPE deposits with increased cholesterol metabolites. (**A**) Representative Oil Red O staining of 12-month-old *Abca1/g1*$^{F/F}$ and *Abca1/g1*$^{-m/-m}$ mice retinas. Note the lipid deposits within the RPE (yellow arrowheads) or subretinal space (red arrowhead). Scale bar: 20μm. (**B**) Analyses of free cholesterol, 3β,5α,6β-cholestanetriol (C-triol), 4β-hydroxycholesterol (4β-HC), 24-hydroxycholesterol (24-HC), 25-HC, 27-HC, and 7-ketocholesterol in retina/RPE/choroid complex at 12 months of age (normalized peak area ratio/mg wet tissue weight). *Abca1/g1*$^{F/F}$, $n = 7$; *Abca1/g1*$^{-m/-m}$, $n = 6$. $^{*}P < 0.05$ and $^{**}P < 0.01$ by 2-tailed unpaired *t* test. (**C**) Analyses of cholesterol esters (CE) in retina/RPE/choroid complex at 12 months of age (normalized peak area ratio/mg wet tissue weight). *Abca1/g1*$^{F/F}$, $n = 7$; *Abca1/g1*$^{-m/-m}$, $n = 6$. $^{**}P < 0.01$ and $^{***}P < 0.001$ by 2-tailed unpaired *t* test. Values are mean ± SEM.

Methods

Supplemental Methods are available online with this article.

Animals. All mice were housed in a temperature-controlled room under a 12-hour light/dark cycle, with free access to food and water. *Abca1*$^{fl/fl}$ *and Abcg1*$^{fl/fl}$ (*Abca1/g* $^{F/F}$) mice were previously characterized (23) and were purchased commercially (The Jackson Laboratory). To generate mice lacking both *Abca1* and *Abcg1* specifically from macrophages, we crossed *Abca1/g1*$^{F/F}$ mice with mice carrying 1 copy of the LysM-Cre transgene, which were purchased commercially (The Jackson Laboratory) and have been previously characterized (17, 21, 23).

RNA isolation and qPCR. Total RNA was extracted using RNeasy Micro Plus kit (Qiagen) according to the manufacturer's instructions. To synthesize cDNA, total RNA was added to the High Capacity cDNA Reverse Transcription Kit (Thermo Fisher Scientific) and reverse-transcribed according to manufacturer's

instructions. qPCR was performed in duplicate using the StepOnePlus Real Time PCR system (Thermo Fisher Scientific) using TaqMan Real-Time PCR Assays (Thermo Fisher Scientific), and the mRNA was quantified using the ΔΔCT method with *gapdh* or *bactin* as the internal control.

Transmission EM. We performed transmission EM as previously described (31). Briefly, for ultrastructural analyses, samples were fixed in 2% paraformaldehyde (PFA)/2.5% glutaraldehyde (Polysciences Inc.) in 100 mM sodium cacodylate buffer, pH 7.2, for 2 hours at room temperature and then overnight at 4°C. Samples were washed in sodium cacodylate buffer at room temperature and postfixed in 1% osmium tetroxide (Polysciences Inc.) for 1 hour. Samples were then rinsed extensively in dH_20 prior to en bloc staining with 1% aqueous uranyl acetate (Ted Pella Inc.) for 1 hour. Following several rinses in dH_2O, samples were dehydrated in a graded series of ethanol and embedded in Eponate 12 resin (Ted Pella Inc.). Sections of 95 nm were cut with a Leica Ultracut UCT ultramicrotome (Leica Microsystems Inc.), stained with uranyl acetate and lead citrate, and viewed on a JEOL 1200 EX transmission electron microscope (JEOL USA Inc.) equipped with an AMT 8 megapixel digital camera and AMT Image Capture Engine V602 software (Advanced Microscopy Techniques).

To measure BrM thickness, we used 25,000× EM pictures. We set 5 measurement points that were arranged at equal 500-nm intervals and measured BrM thickness using Adobe Photoshop CS 5.1 (Adobe). We took averages of each picture as representative BrM thickness.

Electroretinography (ERG). ERG was performed as previously described (32). Briefly, A UTAS BigShot System (LKC Technologies Inc.) was used. Mice were dark adapted overnight. Under red light illumination, mice were anesthetized with an i.p. injection of 86.9 mg/kg ketamine and 13.4 mg/kg xylazine. Pupils were dilated with 1% atropine sulfate eye drops (Bausch & Lomb). Body temperature was maintained at 37°C with a heating pad. Contact lens electrodes were placed bilaterally with appropriate reference and ground electrodes. The stimulus consisted of a full-field white light flash (10 μs) in darkness or in the presence of dim (30.0 candela [cd]/m^2) background illumination after 10-minute adaptation time. Raw data were processed using MATLAB software (MathWorks). The amplitude of the a-wave was measured from the average pretrial baseline to the most negative point of the average trace, and the b-wave amplitude was measured from that point to the highest positive point.

For testing dark adaptation, we modified the protocol as previously described (33). Briefly, we used a UTAS BigShot System (LKC Technologies Inc.) to get scotopic a-waves. A bright LED light (150,000 lux) was applied to both eyes for 15 seconds to photobleach an estimated 90% of the visual pigment. The recovery of the ERG responses was monitored at fixed post-bleach time points within 100 minutes after the bleach. The sensitivity was calculated as the ratio of dim flash response amplitude and the corresponding flash intensity in the linear range of the intensity-response curve. The post-bleach sensitivities were normalized to their dark-adapted prebleach level.

Retinal imaging. We performed digital color fundus photography and OCT as previously described (21) using the Micron III animal fundus camera equipped with 830 nm OCT (Phoenix Research Labs). Prior to fundus imaging and OCT, we anesthetized mice with an i.p. injection of 86.9 mg/kg ketamine and 13.4 mg/kg xylazine and administered 1.0% tropicamide eye drops (Bausch & Lomb) to dilate the pupils.

Cryopreservation. Enucleated posterior poles were fixed in 4% PFA followed by cryopreservation in Tissue-Tek OCT compound (Sakura Finetek). Cryosections (10-μm thick) were cut and collected on gelatin-coated slides and stored at –20°C until use.

ORO staining. ORO (0.7%, MilliporeSigma) staining solution was prepared in 100% propylene glycol (MilliporeSigma) by heating the solution to 90°C. The staining protocol was as follows. Slides were rinsed with water and placed in 100% propylene glycol for 5 minutes, followed by staining overnight in preheated (60°C) ORO solution. Slides were next differentiated in 85% propylene glycol for 1 minute at room temperature, followed by 2 rinses in water. Slides were dried at room temperature, mounted in Aqua-Poly/Mount (Polysciences Inc.), and imaged using a ZEISS Axionplan 2 light microscope.

IHC. Retinal cryosections were incubated with a blocking solution of 10% normal goat serum (NGS) in PBTA (PBS, 0.5% BSA, 0.1% Triton, 0.05% Sodium Azide) for 2 hours at room temperature. After the blocking, sections were probed with either anti-Iba1 (Wako, catalog 019-19741; 1:200 in 10% NGS-PBTA) or anti-F4/80 antibodies (Bio-Rad, catalog MCA497GA; 1:500 in 10% NGS-PBTA) overnight at 4 °C. The next day, anti-Iba1 sections were incubated in goat anti–rabbit-568 (Thermo Fisher Scientific, catalog A11011; 1:200 in 5% NGS-PBTA) and anti-F4/80 sections were incubated in goat anti–rat-568 (Thermo Fisher Scientific, catalog A11077; 1:200 in 5% NGS-PBTA), both for

2 hours at room temperature. Nuclei were counterstained with DAPI (MilliporeSigma). All sections were examined under a confocal microscope equipped with a digital camera (C2si confocal microscope, Nikon Corporation). To count Iba1- or F4/80-positive cells in the subretinal space, 3 slides per animal were stained with Iba1 and F4/80, and 3 equidistant fields of view were identified in the nasal, central, and temporal regions, per slide. The number of staining positive cells were counted in each field of view and their mean was taken (*n*). The *n* values from 3 slide were averaged as cell counts/field in the subretinal space.

Analyses of oxysterols, free cholesterol, and cholesterol esters in retina/RPE/choroid complex. Each retina/RPE/choroid complex was homogenized with 50-fold excess volume of PBS buffer using Omni Bead Ruptor 24 (Omni International Inc.). All analytes listed above in 50 μl of the mouse retina homogenate were extracted with 200 μl of methanol. Prior to the extraction, triol-d7 (2 ng), 7-ketocholesterol-d7 (2 ng), 24-hydroxycholesterol-d7 (24-HC-d7; 2 ng), 27-HC-d5 (2 ng), 4β-HC-d7 (2 ng), cholesterol esters (18:2)-d7 (CE[18:2]-d7;200 ng), and cholesterol-d7 (1 μg) were added as the internal standards to the homogenate samples. All oxysterols and cholesterol, as well as their deuterated standards, were derivatized with N,N-dimethylglycine (DMG) to increase the MS sensitivity. Cholesterol esters were not derivatized for the MS analyses.

Oxysterol analysis was performed with a Shimadzu 20AD HPLC system and a Shimadzu SIL 20AC autosampler coupled to a triple quadrupole mass spectrometer (API-6500Qtrap+, Thermo Fisher Scientific) operated in multiple reaction monitoring (MRM) mode. The positive ion electrospray ionization (ESI) mode was used for detection of the DMG derivatized oxysterols. All samples were injected in duplicate for data averaging. Data processing was conducted with Analyst 1.6.3 (Thermo Fisher Scientific).

The analysis of free cholesterol and 2 CEs (CE[16:0] and CE[18:0]) was performed with a Shimadzu 20AD HPLC system: a LeapPAL autosampler coupled to a triple quadrupole mass spectrometer (API 4000) operated with positive ion MRM mode. The data processing was conducted with Analyst 1.5.1 (Thermo Fisher Scientific).

The analysis of the rest of the CEs (CE[16:2], CE[18:1], CE[18:2], and CE[20:4]) was performed with a Shimadzu 10AD HPLC system and a Shimadzu SIL 20AC autosampler coupled to a triple quadrupole mass spectrometer (TSQ Quantum Ultra) operated in MRM mode. The data processing was conducted with XCalibur.

The relative quantification data is reported as peak area ratios of analytes to their internal standards normalized to wet weights (mg) of retina/RPE/choroid complex.

Statistics. We performed statistical testing with GraphPad Prism (Version 6.0), using the appropriate test for each dataset (2-way ANOVA, 2-way ANOVA with post hoc Bonferroni's multiple comparison test, 2-tailed unpaired *t* test, or 2-tailed Mann-Whitney *U* test). We defined statistical significance as a $P < 0.05$. Values are mean ± SEM.

Study approval. All animal experiments were reviewed and approved by the IACUC of Washington University in St. Louis and performed in accordance with the Washington University School of Medicine Animal Care and Use guidelines.

Author contributions

NB, A. Sene, MC, and RSA designed and analyzed the experiments. NB, TJL, A. Sene, MC, ML, ZD, A. Santeford, and JBL conducted the experiments. NB and RSA wrote the manuscript. GM supervised IHC and ORO staining and contributed to preparation of the manuscript. DSO supervised lipidomic analyses and data analysis and contributed to preparation of the manuscript.

Acknowledgments

We thank Wandy L. Beatty for EM analyses. This work was supported by NIH grants R01 EY019287 (RSA), P30 EY02687 (Vision Core Grant), R01 EY027802 (GM), P30 EY005722 (to the Duke Eye Center); the International Retinal Research Foundation (NB); the Starr Foundation (RSA); the Carl Marshall Reeves and Mildred Almen Reeves Foundation (RSA); the Bill and Emily Kuzma Family Gift for retinal research (RSA); a Physician-Scientist Award and a Nelson Trust Award from Research to Prevent Blindness (RSA); the Jeffrey Fort Innovation Fund (RSA); and the Thome Foundation (RSA). Additional funding came from unrestricted grants to the Department of Ophthalmology and Visual Sciences of Washington University School of Medicine and to the Duke Eye Center, from Research to Prevent Blindness. JBL

was supported by the Washington University in St. Louis Medical Scientist Training Program (NIH grant T32 GM07200) and the Washington University in St. Louis Institute of Clinical and Translational Sciences (NIH grants UL1 TR002345, TL1 TR002344). Lipidomics was performed in the Washington University Metabolomics Facility supported by NIH grant P30 DK020579.

Address correspondence to: Rajendra S. Apte, Center for Outpatient Health, 4901 Forest Park Avenue, 6th Floor, St. Louis, Missouri, USA 63108. Phone: 314.362.3937; Email: apte@wustl.edu.

1. Friedman DS, et al. Prevalence of age-related macular degeneration in the United States. *Arch Ophthalmol*. 2004;122(4):564–572.
2. Khan KN, et al. Differentiating drusen: Drusen and drusen-like appearances associated with ageing, age-related macular degeneration, inherited eye disease and other pathological processes. *Prog Retin Eye Res*. 2016;53:70–106.
3. Sene A, Apte RS. Eyeballing cholesterol efflux and macrophage function in disease pathogenesis. *Trends Endocrinol Metab*. 2014;25(3):107–114.
4. Sene A, Chin-Yee D, Apte RS. Seeing through VEGF: innate and adaptive immunity in pathological angiogenesis in the eye. *Trends Mol Med*. 2015;21(1):43–51.
5. Zweifel SA, Spaide RF, Curcio CA, Malek G, Imamura Y. Reticular pseudodrusen are subretinal drusenoid deposits. *Ophthalmology*. 2010;117(2):303–12.e1.
6. Curcio CA, Messinger JD, Sloan KR, McGwin G, Medeiros NE, Spaide RF. Subretinal drusenoid deposits in non-neovascular age-related macular degeneration: morphology, prevalence, topography, and biogenesis model. *Retina (Philadelphia, Pa)*. 2013;33(2):265–276.
7. Greferath U, Guymer RH, Vessey KA, Brassington K, Fletcher EL. Correlation of Histologic Features with In Vivo Imaging of Reticular Pseudodrusen. *Ophthalmology*. 2016;123(6):1320–1331.
8. Reyes NJ, O'Koren EG, Saban DR. New insights into mononuclear phagocyte biology from the visual system. *Nat Rev Immunol*. 2017;17(5):322–332.
9. Owsley C, et al. Psychophysical evidence for rod vulnerability in age-related macular degeneration. *Invest Ophthalmol Vis Sci*. 2000;41(1):267–273.
10. Curcio CA. Photoreceptor topography in ageing and age-related maculopathy. *Eye (Lond)*. 2001;15(Pt 3):376–383.
11. Haimovici R, Owens SL, Fitzke FW, Bird AC. Dark adaptation in age-related macular degeneration: relationship to the fellow eye. *Graefes Arch Clin Exp Ophthalmol*. 2002;240(2):90–95.
12. Owsley C, Clark ME, McGwin G. Natural History of Rod-Mediated Dark Adaptation over 2 Years in Intermediate Age-Related Macular Degeneration. *Transl Vis Sci Technol*. 2017;6(3):15.
13. Neale BM, et al. Genome-wide association study of advanced age-related macular degeneration identifies a role of the hepatic lipase gene (LIPC). *Proc Natl Acad Sci USA*. 2010;107(16):7395–7400.
14. Chen W, et al. Genetic variants near TIMP3 and high-density lipoprotein-associated loci influence susceptibility to age-related macular degeneration. *Proc Natl Acad Sci USA*. 2010;107(16):7401–7406.
15. Cheung CMG, et al. Plasma lipoprotein subfraction concentrations are associated with lipid metabolism and age-related macular degeneration. *J Lipid Res*. 2017;58(9):1785–1796.
16. Calippe B, et al. Complement Factor H Inhibits CD47-Mediated Resolution of Inflammation. *Immunity*. 2017;46(2):261–272.
17. Sene A, et al. Impaired cholesterol efflux in senescent macrophages promotes age-related macular degeneration. *Cell Metab*. 2013;17(4):549–561.
18. Espinosa-Heidmann DG, Suner IJ, Hernandez EP, Monroy D, Csaky KG, Cousins SW. Macrophage depletion diminishes lesion size and severity in experimental choroidal neovascularization. *Invest Ophthalmol Vis Sci*. 2003;44(8):3586–3592.
19. Edwards AO, Ritter R, Abel KJ, Manning A, Panhuysen C, Farrer LA. Complement factor H polymorphism and age-related macular degeneration. *Science*. 2005;308(5720):421–424.
20. Wang X, et al. Macrophage ABCA1 and ABCG1, but not SR-BI, promote macrophage reverse cholesterol transport in vivo. *J Clin Invest*. 2007;117(8):2216–2224.
21. Santeford A, et al. Impaired autophagy in macrophages promotes inflammatory eye disease. *Autophagy*. 2016;12(10):1876–1885.
22. Mattapallil MJ, et al. The Rd8 mutation of the Crb1 gene is present in vendor lines of C57BL/6N mice and embryonic stem cells, and confounds ocular induced mutant phenotypes. *Invest Ophthalmol Vis Sci*. 2012;53(6):2921–2927.
23. Westerterp M, et al. Deficiency of ATP-binding cassette transporters A1 and G1 in macrophages increases inflammation and accelerates atherosclerosis in mice. *Circ Res*. 2013;112(11):1456–1465.
24. Clausen BE, Burkhardt C, Reith W, Renkawitz R, Förster I. Conditional gene targeting in macrophages and granulocytes using LysMcre mice. *Transgenic Res*. 1999;8(4):265–277.
25. Abram CL, Roberge GL, Hu Y, Lowell CA. Comparative analysis of the efficiency and specificity of myeloid-Cre deleting strains using ROSA-EYFP reporter mice. *J Immunol Methods*. 2014;408:89–100.
26. Klein R, Klein BE, Franke T. The relationship of cardiovascular disease and its risk factors to age-related maculopathy. The Beaver Dam Eye Study. *Ophthalmology*. 1993;100(3):406–414.
27. Klein R, Klein BE, Jensen SC. The relation of cardiovascular disease and its risk factors to the 5-year incidence of age-related maculopathy: the Beaver Dam Eye Study. *Ophthalmology*. 1997;104(11):1804–1812.
28. Delcourt C, et al. Associations of cardiovascular disease and its risk factors with age-related macular degeneration: the POLA study. *Ophthalmic Epidemiol*. 2001;8(4):237–249.
29. Klein R, Klein BE, Tomany SC, Cruickshanks KJ. The association of cardiovascular disease with the long-term incidence of age-related maculopathy: the Beaver Dam Eye Study. *Ophthalmology*. 2003;110(6):1273–1280.
30. Paun CC, et al. Genetic Variants and Systemic Complement Activation Levels Are Associated With Serum Lipoprotein Levels

in Age-Related Macular Degeneration. *Invest Ophthalmol Vis Sci*. 2015;56(13):7766–7773.
31. Lin JB, et al. NAMPT-Mediated NAD(+) Biosynthesis Is Essential for Vision In Mice. *Cell Rep*. 2016;17(1):69–85.
32. Rajagopal R, Bligard GW, Zhang S, Yin L, Lukasiewicz P, Semenkovich CF. Functional Deficits Precede Structural Lesions in Mice With High-Fat Diet-Induced Diabetic Retinopathy. *Diabetes*. 2016;65(4):1072–1084.
33. Xue Y, Shen SQ, Corbo JC, Kefalov VJ. Circadian and light-driven regulation of rod dark adaptation. *Sci Rep*. 2015;5:17616.